

# Texture/Microstructural Evolution and Mechanical Properties of a Hot and Cold Rolled Al-Mg-Si-Cu Alloy

Yihan Wang, Lixin Zhang, Xiaohui Yang, Kai Li, Song Ni\*, Yong Du, Min Song

State Key Laboratory of Powder Metallurgy, Central South University, Changsha, China

Email: \*song.ni@csu.edu.cn

**How to cite this paper:** Wang, Y.H., Zhang, L.X., Yang, X.H., Li, K., Ni, S., Du, Y. and Song, M. (2017) Texture/Microstructural Evolution and Mechanical Properties of a Hot and Cold Rolled Al-Mg-Si-Cu Alloy. *Journal of Minerals and Materials Characterization and Engineering*, 5, 209-222.  
<https://doi.org/10.4236/jmmce.2017.54018>

**Received:** May 31, 2017

**Accepted:** July 4, 2017

**Published:** July 7, 2017

Copyright © 2017 by authors and Scientific Research Publishing Inc.  
This work is licensed under the Creative Commons Attribution International License (CC BY 4.0).

<http://creativecommons.org/licenses/by/4.0/>



Open Access

## Abstract

The evolutions of texture, microstructure as well as mechanical properties of an Al-Mg-Si-Cu alloy during hot and cold rolling were investigated by TEM, EBSD and X-ray diffraction in this study. The results revealed that formation of sub-grain boundaries and  $<110>/\text{RD}$  fiber texture after hot rolling is beneficial to the increase of the elongation of the alloy. The shear texture of  $<110>/\text{RD}$  fiber and  $\gamma$ -fiber occupies a dominant role during the hot rolling process, while the main texture during the cold rolling process is the rolling texture of  $\beta$ -fiber.  $\beta$ -fiber and  $\tau$ -fiber texture components are identified as two main types of texture components during cold rolling, and the Brass component  $\{011\}<211>$  is transformed into Goss component  $\{011\}<100>$  with the increase of the deformation.

## Keywords

EBSD, Microstructure, Texture Evolution, Mechanical Properties, ODFs

## 1. Introduction

Al-Mg-Si-Cu based alloys are widely used in automotive and aerial industries due to their high strength, good formability, excellent corrosion resistance and anti-fatigue performance, particularly their high strength to weight ratio [1] [2] [3].

Previous investigations showed that the crystallographic texture has a great effect on the formability of aluminum sheet products [4] [5]. It has also been reported that the crystallographic texture affects significantly the tensile properties of aluminum alloys [6] [7] [8] [9] [10]. Chen *et al.* [8] found that the yield strength and ultimate tensile strength of an X2095 alloy along the transverse direction (TD) were higher than those along the longitudinal direction (LD). The

specimens along the L-T orientation exhibited higher fatigue thresholds and lower crack propagation rates due to the occurrence of the textures composed of Brass, Copper and S components, with the Brass texture being the dominant component. Some researchers have demonstrated that the evolution of crystallographic texture during thermo-mechanical processing of aluminum alloy is mainly a  $\beta$ -fiber texture, which evolves from the Copper orientation through the S orientation to the Brass orientations [11] [12] [13] [14] [15].

In general, texture evolution can be affected by many factors, such as alloy composition, deformation temperature, deformation degree, lubricant condition, thermomechanical processing conditions, intermediate annealing, heat treatment and others [4] [16] [17] [18] [19]. However, the relationship between the microstructure, texture evolution and mechanical properties of Al-Mg-Si-Cu alloys during hot/cold rolling deformation is still not well understood. Hence, this study is aimed to understand the effect of hot and cold rolling on the microstructure, texture evolution and mechanical properties of an Al-Mg-Si-Cu alloy, and provide guidance for the optimization of the processing method.

## 2. Experimental Procedures

The material used in this investigation was an as-cast Al-Mg-Si-Cu alloy prepared from pure Al (99.9 wt.%), pure Mg (99.9 wt%), master alloys of Al-20Si (wt.%) and Al-50Cu (wt.%) by a medium frequency induction furnace. The chemical composition of the alloy, which was determined by inductively coupled plasma atomic emission spectroscopy (ICP-AES), is shown in **Table 1**. The initial samples with a size of 120 mm (length)  $\times$  40 mm (width)  $\times$  10 mm (thickness) was cut from the ingot after homogenization annealing at 555°C for 20 h. Subsequently, the sheets were pre-heated in a muffle furnace at 450°C for 1 hour. Then a two-step hot rolling was carried out on the samples: hot rolling from 10 mm to 7 mm (with a 30% reduction, denoted as HR7), and then further hot rolling to 5 mm (with a 50% reduction in total, denoted as HR5) at 450°C. After hot rolling, the HR5 samples were further subject a two-step cold rolling: cold rolling to 3 mm (with a 70% reduction in total, denoted as HR+CR3) and then further cold rolling to 1mm (with a 90% reduction in total, denoted as HR+CR1) at room temperature. The tensile properties of the alloy was tested using an Instron 3369 testing machine with a cross speed of  $1.67 \times 10^{-5}$  m·s<sup>-1</sup>. The tensile samples with 26 mm in gauge length and 10 mm in diameter were prepared along three different directions, which have 0° (rolling direction, RD), 45° (inclined direction, ID) and 90° (transverse direction, TD) to the rolling direction of the sheets. The microstructures of the samples were investigated using a JEOL-2100F transmission electron microscope (TEM) operated at 200 KV. The TEM specimens were prepared firstly by mechanical grinding and then twin-jet

**Table 1.** Chemical composition of the as-cast Al-Mg-Si-Cu alloy.

Element	Mg	Si	Cu	Fe	Cr	Ni	Zn	Al
wt.%	0.80	0.80	0.66	0.10	0.12	0.038	0.023	Bal.

polishing in a solution of 30% nitric acid and 70% methanol at  $-30^{\circ}\text{C}$ . The orientation of the grains and the microstructural evolution were determined by an electron backscatter diffraction (EBSD) system mounted on an FEI Quanta FEG 250 scanning electron microscope (SEM) with a field emission gun. The specimens for EBSD (RD-TD plane) were firstly mechanically grinded and then electrochemically polished by a direct current (DC) supplying power stably at 20 V for 15 - 30 s. The electrolyte was composed of 25% nitric acid and 75% carbinol. The macrotexture was measured by X-ray diffraction (XRD). The (111), (200) and (220) incomplete pole figures were measured by a PANalytical X' Pert-PRO MRD X-ray diffractometer. The orientation distribution functions (ODFs) were calculated from the three incomplete pole figures obtained through Schulz back reflection method using Cu K $\alpha$  radiation. The main texture components of the ODFs were quantitatively analyzed by calculating the volume fraction.

### 3. Results

#### 3.1 Microstructure

**Figure 1** shows the EBSD maps of the HR7, HR5, HR+CR3 and HR+CR1 samples. Colors used in the figure represent various orientations in the interior of the grains, corresponding to the inverse pole figure (IPF) inserted in **Figure 1(d)**. In the orientation maps, the grain boundaries were divided into high-angle grain boundaries (HAGBs, with misorientation between  $15^{\circ}$  -  $180^{\circ}$ ) and low-angle grain boundaries (LAGBs, with misorientation between  $2^{\circ}$  -  $15^{\circ}$ ). The average grain sizes of the HR7 and HR5 specimens are  $1.5 \times 0.8$  mm (length  $\times$  width) and  $2 \times 1.6$  mm (length  $\times$  width), respectively. Color gradient in the large-sized grain interior can be observed in both HR7 and HR5 specimens (**Figure 1(a)** and **Figure 1(b)**). It indicates that strain gradient is produced in the grain interior due to defects pile-up during the hot-rolling deformation and therefore generated misorientation within the grains before these grains are divided into subgrains [20]. **Figure 1(c)** indicated that the grain pattern of HR + CR3 sample was the elongated grains along the rolling direction after cold rolling. The microstructure of the final cold rolled alloy in **Figure 1(d)** shows that the elongated grains were severely broken into many equiaxed grains. This is confirmed by the results of the grains boundary misorientations (**Figure 2**), which showed that the fraction of the misorientation ( $>10^{\circ}$ ) increases gradually as the rolling reduction increases, from sample HR7 to HR+CR1 (see **Figure 2**).

**Figures 3(a)-(d)** show the misorientation of the corresponding regions in **Figures 1(a)-(d)**. The red and green lines represent the grain boundary angles of  $2^{\circ}$  -  $5^{\circ}$  and  $5^{\circ}$  -  $15^{\circ}$  (LAGBs), respectively, and the blue lines represent the grain boundary angle of  $15^{\circ}$  -  $180^{\circ}$  (HAGBs). **Table 2** provides the average misorientation and the volume fraction of three types of misorientation angles in **Figure 3**. It can be seen from **Table 2** that the average misorientation decreases firstly from sample HR7 to sample HR5 and then increases from sample HR 5 to sample HR+CR1. The reason can be explained by the TEM bright field images of

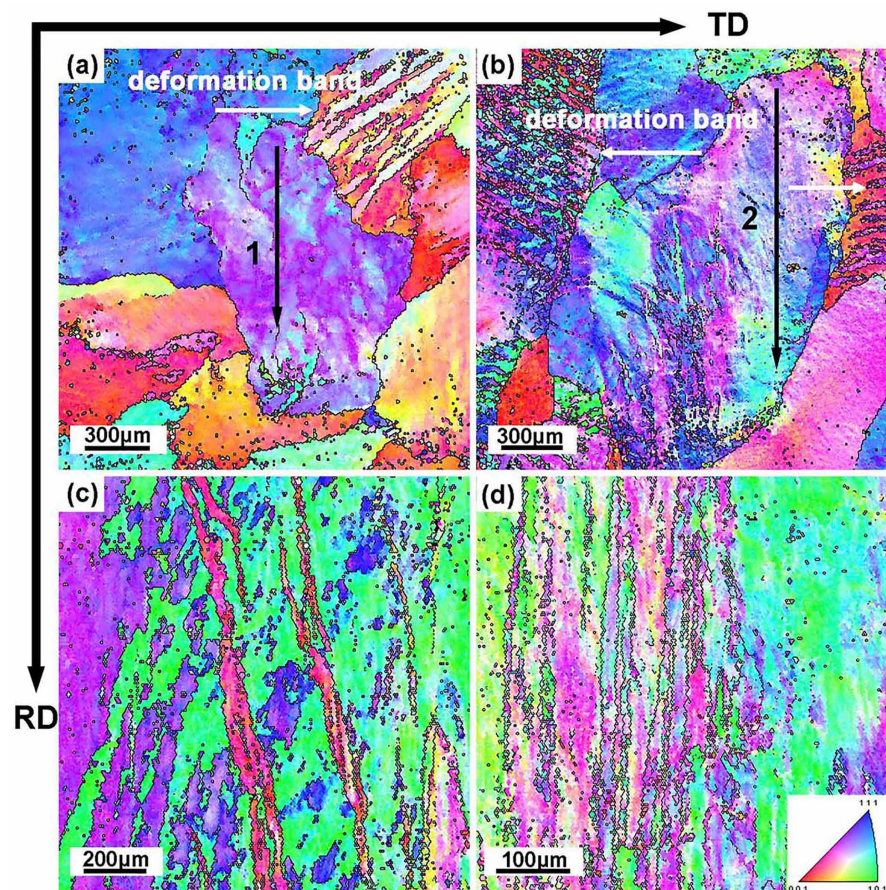


**Figure 1.** EBSD maps of (a) HR7, (b) HR5, (c) HR+CR3 and (d) HR+CR1 samples.

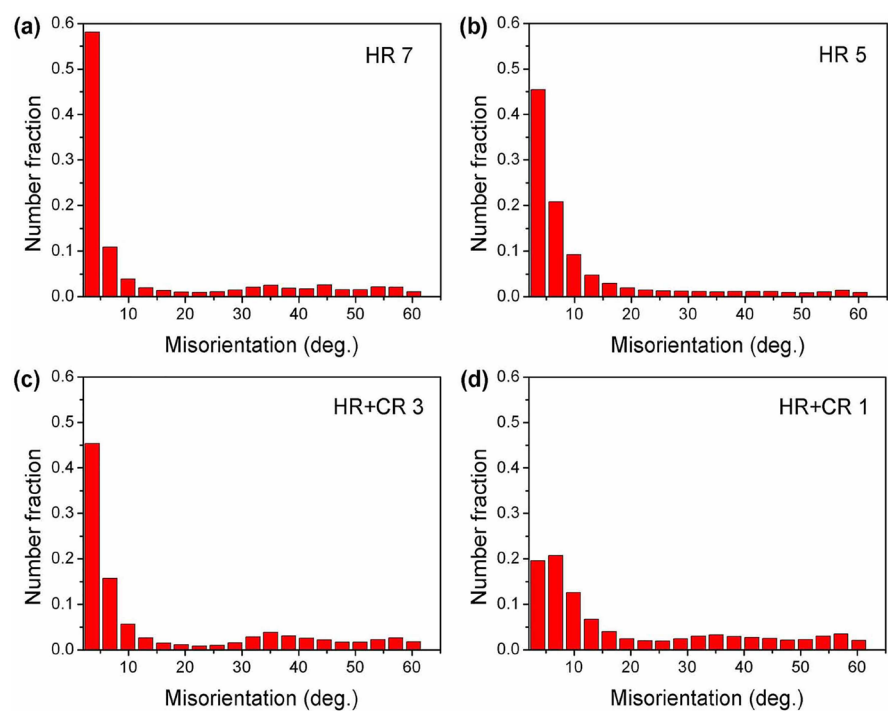


**Figure 2.** The grain boundary misorientations for (a) HR7, (b) HR5, (c) HR+CR3 and (d) HR+CR1 samples.

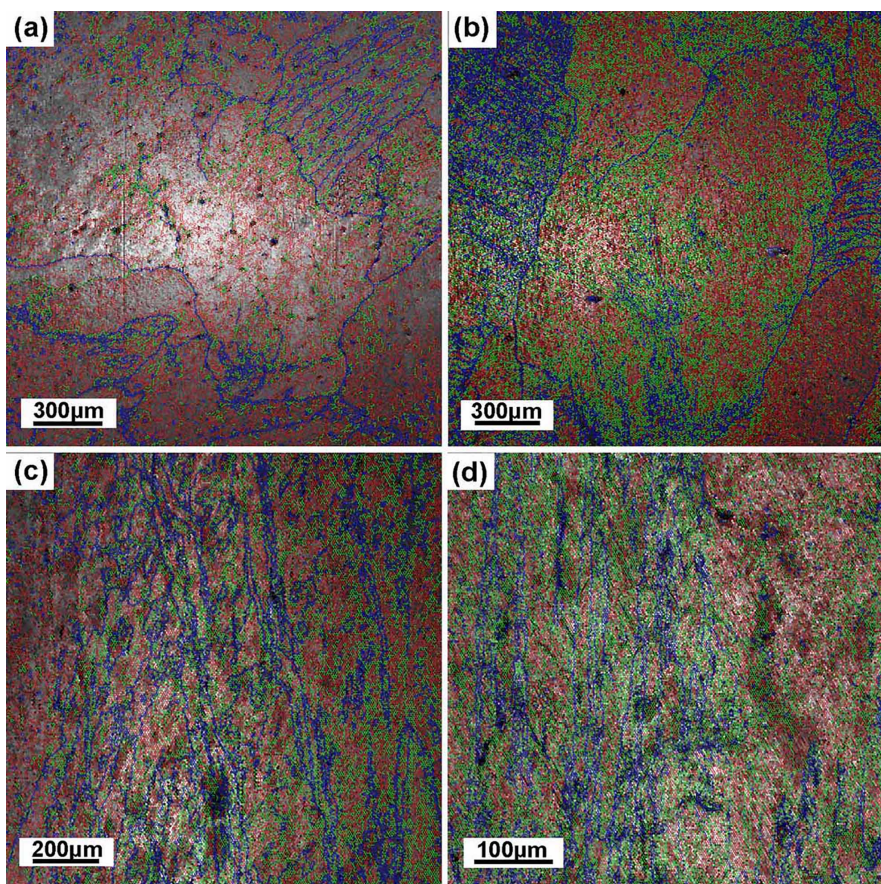


**Figure 3.** Misorientations of (a) HR7, (b) HR5, (c) HR+CR3 and (d) HR+CR1 samples. The red lines represent the grain boundary angle of  $2^\circ$  -  $5^\circ$ , the green lines represent the grain boundary angle of  $5^\circ$  -  $15^\circ$ , and the blue lines represent the grain boundary angle of  $15^\circ$  -  $180^\circ$ .

**Table 2.** Grain boundary misorientation of the four samples.

Sample	Rotation Angle (deg.)	Fraction (%)	Average Angle (deg.)
HR7	2 - 5	56.0	13.17
	5 - 15	17.4	
	15 - 180	26.6	
HR5	2 - 5	45.4	11.26
	5 - 15	35.7	
	15 - 180	18.9	
HR+CR3	2 - 5	48.8	15.68
	5 - 15	29.9	
	15 - 180	21.3	
HR+CR1	2 - 5	42.7	19.49
	5 - 15	41.0	
	15 - 180	16.3	

Legend: for statistics, any point pair with misorientation exceeding  $2^\circ$  is considered a boundary.

the Al-Mg-Si-Cu alloy sheets after different rolling reductions, as shown in **Figure 4**. For the sheet HR7, a mass of subgrains with few dislocations can be clearly observed after the first step of hot rolling (**Figure 4(a)**). After the second step of hot rolling, subgrains can still be observed, accompanied by a large number of the dislocations in the subgrains of sheet HR5 (**Figure 4(b)**). Therefore, the increase of the dislocations in subgrains caused the decrease of the average misorientation from sample HR7 to sample HR5. Furthermore, after two steps of cold rolling, the grains were elongated firstly (**Figure 4(c)**), and then a small number of the equiaxed grains were formed (**Figure 4(d)**). With increasing the strain, the grains are refined to some extent, making subgrain boundaries gradually transform from LAGBs to HAGBs. Hence, the average misorientation increases from sample HR 5 to sample HR+CR1.

**Figure 5** shows the misorientation profiles of point-to-point (red line) and point-to-origin (blue line) of vector 1 in **Figure 1(a)** and vector 2 in **Figure 1(b)** along the rolling direction. In **Figure 5(a)**, the misorientation profile of point-to-point shows only a slight fluctuation belonging to LAGBs. From the accumulated misorientation profile of point-to-origin, the regions of vector 1 in the large grain (in **Figure 1(a)**) along the rolling direction have a maximum misorientation of about  $16^\circ$ . In **Figure 5(b)**, the misorientation profile of point-to-point displays a more dramatic fluctuation. Moreover, in the accumulated misorientation profile of point-to-origin, a continuous increase of about  $5^\circ - 27^\circ$  has been observed. This phenomenon reveals that defects pile-up in the sample HR5 is more serious than in the sample HR7, in consistent with **Figure 4(a)-(b)**.

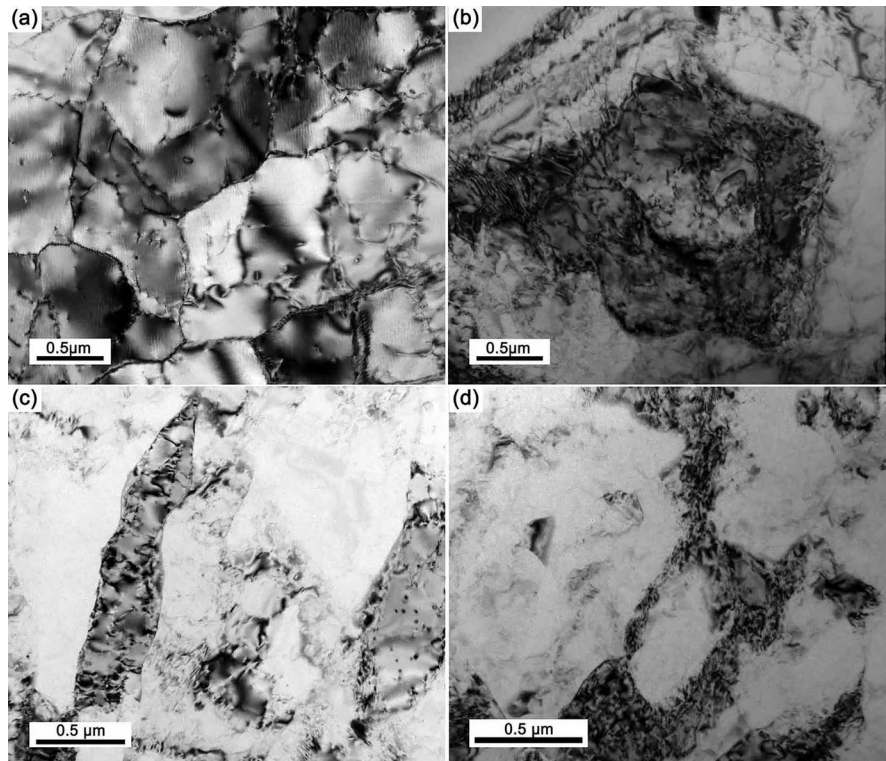


**Figure 4.** Bright field TEM images of (a) HR7, (b) HR5, (c) HR+CR3 and (d) HR+CR1 samples.

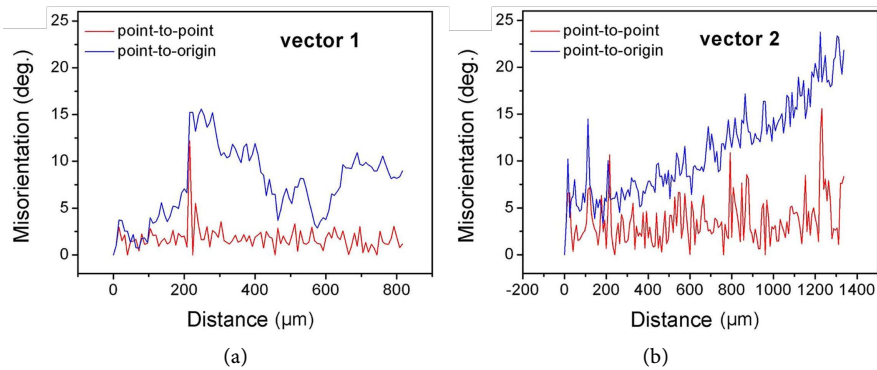


**Figure 5.** Misorientations along vectors (a) 1 and (b) 2 in two elongated grains along the rolling direction shown in **Figure 1(a)** and **Figure 1(b)**, respectively. The red lines represent point-to-point misorientation, whereas the blue lines represent point-to-origin misorientation.

### 3.2. Texture Evolution

**Figure 6** shows the texture evolution of the samples before and after hot and cold rolling, by plotting the ODFs in four characteristic sections with  $\psi_2 = 0^\circ$ ,  $45^\circ$ ,  $65^\circ$  and  $90^\circ$  through the Euler orientation space. The main textures in the as-annealed sample are characterized by Cube and Brass components (**Figure 6(a)**). As shown in **Figure 6(b)**, the textures for sample HR7 are mainly characterized by a  $<110>/RD$  fiber texture, which runs from the Rotated Cube orientation through the Inverse Brass orientation to the E orientation, a weak F orientation and a weak Copper orientation. There is a gradual increasing trend in the  $\gamma$ -fiber texture, which runs from the E orientation through the F orientation by increasing hot-rolling reduction from 30% to 50% (as shown in **Figure 6(c)**).

Simultaneously, the intensities of the Inverse Brass and Rotated Cube textures show a remarkably decrease for the sample HR5. After cold rolling, the texture is composed of the D (Dillamore)  $<11118>$  orientation and a  $\beta$ -fiber that extends through the Copper, S and Brass orientations (**Figure 6(d)**). Here, the S orientation exhibits the largest intensity along the  $\beta$ -fiber. After the last step of the cold rolling, the D component and the  $\beta$ -fiber texture carried over from sample HR+CR3 can still be observed but the intensity of them both decreased sharply.

The texture results are further summarized in **Figure 7** by measuring the fraction of the main texture components. **Figure 7(a)** shows the volume fraction of ten types of texture components during the rolling deformation process. **Figure 7(b)** displays the evolution of recrystallization texture during hot and cold rolling. The bulk texture after hot-rolling with a 30% and 50% reduction is typical of significant shear deformation, which comprised of E, F, Rotated Cube and Inverse Brass orientations (**Figure 7(c)**). It is worth mentioning that the shear texture components of Rotated Cube and Inverse Brass occupied a dominant role after HR7 hot-rolling. On the contrary, the E and F components played leading role after the HR5 hot-rolling. Meanwhile, the volume fraction of Rotated Cube and Inverse Brass components is significantly reduced. After two steps of cold-rolling, the texture comprises rolling orientations with strong S and

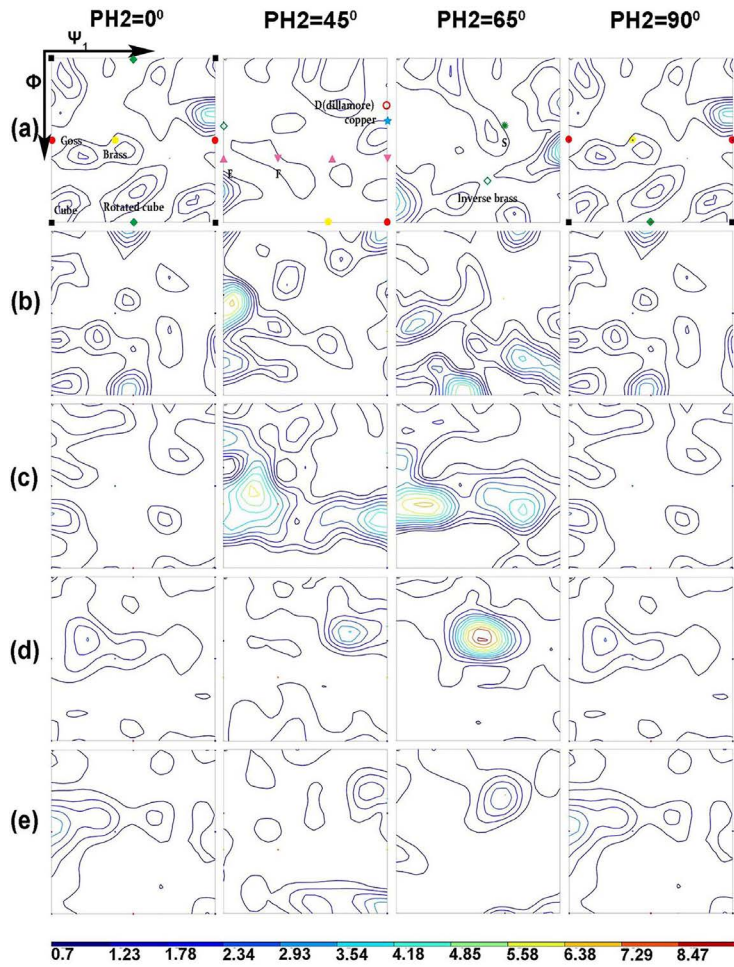


**Figure 6.** ODFs of (a) as-homogenization annealed sample; (b) HR7; (c) HR5; (d) HR + CR3 and (e) HR + CR1 samples.

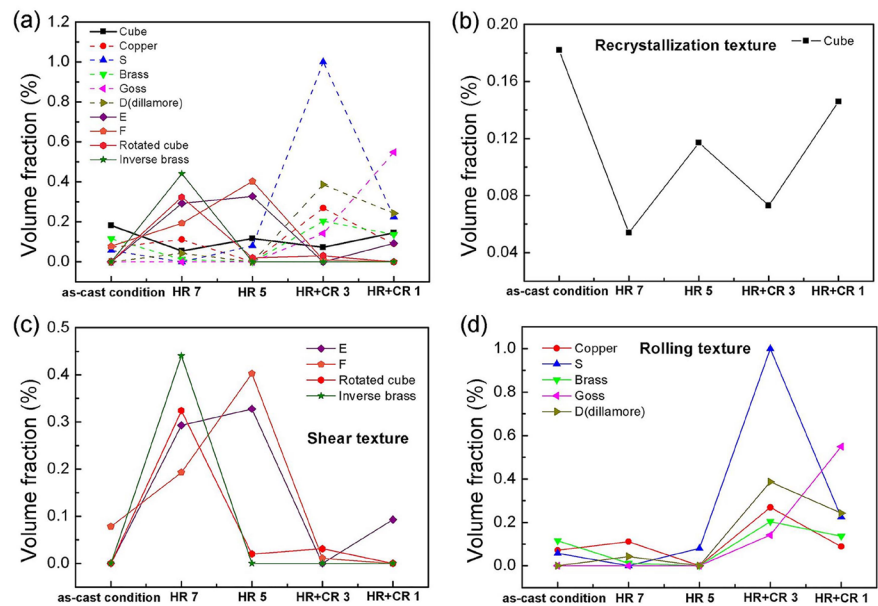


**Figure 7.** Volume fractions of the main texture components in the rolled Al-Mg-Si-Cu alloy.

weak Copper, Brass, Goss and D (Dillamore) components, and the absence of any orientations typical of shear (**Figure 7(d)**). Along the whole hot and cold rolling process, the volume fraction of Cube orientation (a kind of recrystallization textures) shows a minor fluctuation.

### 3.3. Mechanical Properties

**Figure 8** shows the engineering stress-strain curves of the rolled Al-Mg-Si-Cu alloy from three different directions. It can be seen that the evolution characteristics are similar along three directions with increasing the rolling deformation degree. It is evident that the tensile strength increases and the elongation decreases during the rolling process, except for sample HR7. After the first step of hot rolling, the fracture elongation values increased from 25.7% to 38.8% along the  $0^\circ$  (RD) direction, 25.5% to 41% along the  $45^\circ$  direction and 25.4% to 39.7% along the  $90^\circ$  (TD) direction, respectively.

**Figure 9** shows the engineering stress-strain curves of the Al-Mg-Si-Cu alloy along three different directions after different rolling deformation. The result

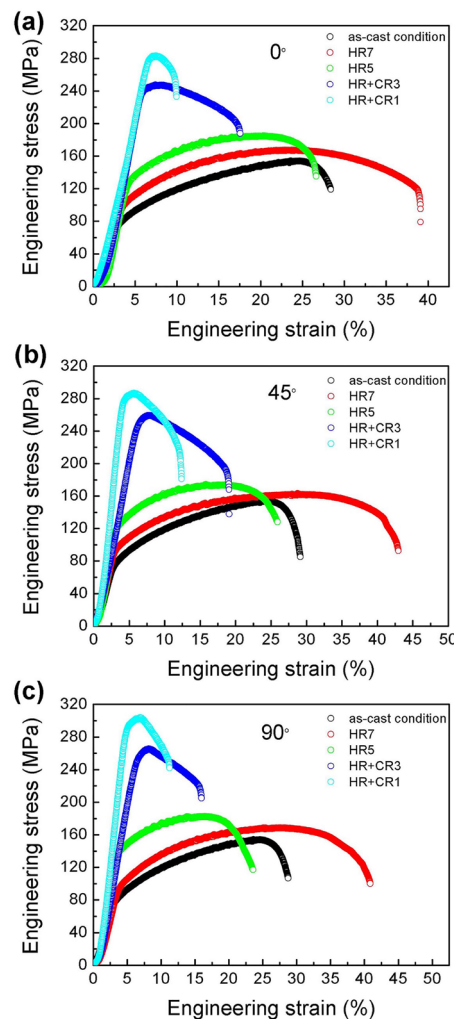


**Figure 8.** Engineering stress-strain curves of the rolled Al-Mg-Si-Cu alloy along different directions to the rolling direction: (a)  $0^\circ$ ; (b)  $45^\circ$ ; (c)  $90^\circ$ .

reveals that the mechanical property anisotropy is weak for sample HR7 (**Figure 9(a)**). The elongation and tensile strength along  $0^\circ$  (RD) direction of sample HR5 is higher than that along the other two directions. For cold rolled samples, the elongation along  $45^\circ$  direction has the highest values, and the tensile strength and the yield strength along the  $90^\circ$  (TD) direction is larger than those along the other directions (**Figures 9(c)-(d)**).

## 4. Discussion

### 4.1. Microstructure

As shown in **Figure 1**, the grain morphology changed gradually from near-equiaxed shape to elongated shape during the rolling process. After the final cold rolling, some of the elongated grains were ultimately broken into many equiaxed small grains. In addition, from sample HR7 to sample HR+CR1, the fraction of HAGBs gradually increases with increasing the rolling reduction (as shown in **Figure 2**). After two steps of hot rolling, a slight number of the LAGBs can be observed inside the initially large-sized grains, and the LAGBs increased obviously with increasing the rolling reduction (as shown in **Figure 3(a)** and **Figure 3(b)**). **Table 2** also indicates that the fraction of  $2^\circ$  -  $5^\circ$  LAGBs has the largest value in all the grain boundaries with different angles during the four rolling states. However, it is worth mentioning that the fraction of  $5^\circ$  -  $15^\circ$  grain boundaries increases from 17.4% to 35.7% and  $15^\circ$  -  $180^\circ$  grain boundaries decreases from 26.6% to 18.9% with increasing the hot rolling reduction. Similarly, the fraction of  $5^\circ$  -  $15^\circ$  grain boundaries increases from 29.9% to 41% and  $15^\circ$  -  $180^\circ$  grain boundaries decreases from 21.3% to 16.3% with increasing the cold rolling reduction. This is due to the fact that the formation speed of the LAGBs is faster

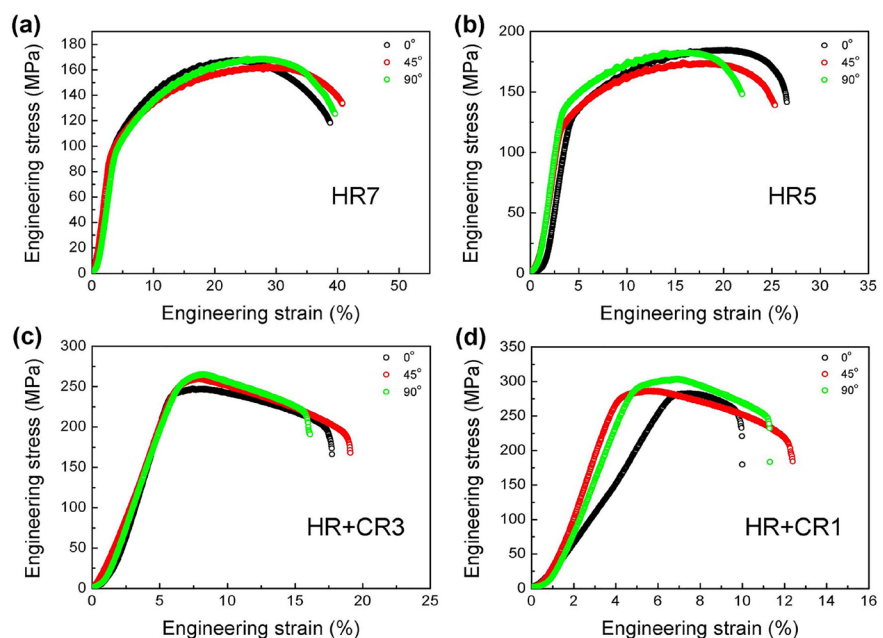


**Figure 9.** Engineering stress-strain curves of the rolled Al-Mg-Si-Cu alloy under different rolling state: (a) HR7; (b) HR5; (c) HR + CR3 and (d) HR + CR1.

than that of the HAGBs during hot/cold rolling. During hot-rolling deformation, strain gradient is produced in the grain interior due to defects pile-up and therefore generated misorientation within the grains before these grains are divided into subgrains. This is in consistent with the value of average misorientation angle in **Table 2**: the average misorientation angle decreases from sample HR7 to HR5. Although the presented region (**Figure 1(a)** and **Figure 1(b)**) is limited and only several crystal grain were observed, the other regions show similar characteristics.

#### 4.2. Texture

Based on the present results, the general evolution of textures in RD-TD planes of the alloy plates during hot and cold rolling is as follows (see **Figure 6** and **Figure 7**): (i) at as-cast condition, it presents a random orientation, (ii) after the first step of hot rolling, it mainly contains  $<110>/\text{RD}$  fiber texture with weak F and Copper components, (iii) after the second step of hot rolling, it evolved into  $\gamma$ -fiber texture, (iv) after the first step of cold rolling, it has strong  $\beta$ -fiber and  $\tau$ -fiber texture with the S component having the highest intensity, (v) after the final cold rolling, it evolved into  $\tau$ -fiber texture and weak  $\beta$ -fiber texture with the Goss component having the highest intensity.

As reported previously that the generation of shear strain leads to the formation of shear texture [21] [22] [23]. Obviously, the two kinds of shear texture,  $<110>/\text{RD}$  fiber and  $\gamma$ -fiber have a dominant role during hot rolling process. Furthermore, Copper component, a relatively weak rolling texture, has been generated after HR7 hot rolling process. After HR+CR3 cold rolling process,  $<110>/\text{RD}$  fiber and  $\gamma$ -fiber disappear rapidly and strong  $\beta$ -fiber and  $\tau$ -fiber are generated. It has been reported that the final cold rolling deformation has a great influence on the texture evolution [10]. Compared to HR+CR3 cold rolling state,  $\beta$ -fiber disappears and the highest component intensity of  $\tau$ -fiber has been defined as Goss texture after the final cold rolling.

#### 4.3. Mechanical Properties

Normally, the increase of the strength of aluminum alloy is accompanied by the decrease of the elongation. However, after the first step of hot rolling, the elongation increases from 25.7% to 38.8%, 25.5% to 41%, and 25.4% to 39.7% along the 0°, 45° and 90° directions, respectively. This phenomenon may be explained as follows: on one hand, a lot of sub-grain boundaries were generated inside the large-sized grains after the first step of hot rolling (see **Figure 4(a)**). It has been shown that the formation of sub-grain boundaries was beneficial to the elongation of aluminum alloy [24]. On the other hand, the generation of  $<110>/\text{RD}$  fiber texture promotes the improvement of the elongation of the alloy after the first step of hot rolling [25].

### 5. Conclusions

The evolution of texture, microstructure and mechanical properties of an Al-

Mg-Si-Cu alloy during hot and cold rolling were investigated by TEM, EBSD, X-ray diffraction, with the following conclusions being drawn:

- (1) The shear texture of  $<110>/\text{RD}$  fiber and  $\gamma$ -fiber occupies a dominant role during the hot rolling process, while the main texture during the cold rolling process is the rolling texture of  $\beta$ -fiber.
- (2) The formation of sub-grain boundaries and  $<110>/\text{RD}$  fiber texture after hot rolling is beneficial to the increase of the elongation of the alloy.
- (3)  $\beta$ -fiber and  $\tau$ -fiber texture components are identified as two main types of texture components during the cold rolling process, and the Brass component  $\{011\}<211>$  is transformed into Goss component  $\{011\}<100>$  with increasing the rolling reduction.

## Acknowledgements

The financial support from National Natural Science Foundation of China (51531009) is appreciated.

## References

- [1] Miller, W.S., Zhuang, L., Bottema, J., Wittebrood, A.J., De Smet, P., Haszler, A. and Vieregge, A. (2000) Recent Development in Aluminium Alloys for the Automotive Industry. *Materials Science and Engineering A*, **280**, 37-49.  
[https://doi.org/10.1016/S0921-5093\(99\)00653-X](https://doi.org/10.1016/S0921-5093(99)00653-X)
- [2] Hirsch, J. (2014) Recent Development in Aluminium for Automotive Applications. *Transaction of Nonferrous Metals Society of China*, **24**, 1995-2002.  
[https://doi.org/10.1016/S1003-6326\(14\)63305-7](https://doi.org/10.1016/S1003-6326(14)63305-7)
- [3] Hirsch, J. and Al-Samman, T. (2013) Superior Light Metals by Texture Engineering: Optimized Aluminum and Magnesium Alloys for Automotive Applications. *Acta Materialia*, **61**, 818-843. <https://doi.org/10.1016/j.actamat.2012.10.044>
- [4] Wang, K.F., He, B.Y., Carsley, J.E., Raghavan, R.S., Li, J.J., Hartfield-Wünsch, S.E. and Zhang, L.-H. (2014) Structure-Property Characterization of an Age Hardenable Al-Mg-Si Alloy after Straining and Flash Annealing. *Materials Science and Engineering A*, **595**, 25-33. <https://doi.org/10.1016/j.msea.2013.11.046>
- [5] Barnwal, V.K., Raghavan, R., Tewari, A., Narasimhan, K. and Mishra, S.K. (2017) Effect of Microstructure and Texture on Forming Behaviour of AA-6061 Aluminium Alloy Sheet. *Materials Science and Engineering A*, **679**, 56-65.  
<https://doi.org/10.1016/j.msea.2016.10.027>
- [6] Vasudevan, A.K., Przystupa, M.A. and Fricke Jr., W.G. (1990) Texture-Microstructure Effects in Yield Strength Anisotropy of 2029 Sheet Alloy. *Scripta Materialia*, **24**, 1429-1434. [https://doi.org/10.1016/0956-716X\(90\)90409-A](https://doi.org/10.1016/0956-716X(90)90409-A)
- [7] Marcus, A.M. and Adams, B.L. (1992) Texture Effects on Yield Strength in Aluminium with Variable Grain Volume Distribution. *Scripta Materialia*, **27**, 155-159.  
[https://doi.org/10.1016/0956-716X\(92\)90105-N](https://doi.org/10.1016/0956-716X(92)90105-N)
- [8] Chen, D.L., Chaturvedi, M.C., Goel, N. and Richards, N.L. (1999) Fatigue Crack Growth Behavior of X2095 Al-Li Alloy. *International Journal of Fatigue*, **21**, 1079-1086. [https://doi.org/10.1016/S0142-1123\(99\)00087-0](https://doi.org/10.1016/S0142-1123(99)00087-0)
- [9] Wang, Z.G., Zhang, Z.F., Li, X.W., Jia, W.P. and Li, S.X. (2001) Orientation Dependence of the Cyclic Deformation Behavior and the Role of Grain Boundaries in Fatigue Damage in Copper Crystals. *Materials Science and Engineering A*, **319-321**, 63-73. [https://doi.org/10.1016/S0921-5093\(01\)01055-3](https://doi.org/10.1016/S0921-5093(01)01055-3)

- [10] Wang, X.F., Guo, M.X., Zhang, Y., Xing, H., Li, Y., Luo, J.R., Zhang, J.S. and Zhuang, L.Z. (2016) The Dependence of Microstructure, Texture Evolution and Mechanical Properties of Al-Mg-Si-Cu Alloy Sheet on Final Cold Rolling Deformation. *Journal of Alloys and Compounds*, **657**, 906-916.  
<https://doi.org/10.1016/j.jallcom.2015.10.070>
- [11] Wang, X.F., Guo, M.X., Cao, L.Y., Luo, J.R., Zhang, J.S. and Zhuang, L.Z. (2015) Influence of Thermomechanical Processing on Microstructure, Texture Evolution and Mechanical Properties of Al-Mg-Si-Cu Alloy Sheets. *Transactions of Nonferrous Metals Society of China*, **25**, 1752-1762.  
[https://doi.org/10.1016/S1003-6326\(15\)63780-3](https://doi.org/10.1016/S1003-6326(15)63780-3)
- [12] Yang, W.C., Ji, S.X., Li, Z. and Wang, M.P. (2015) Grain Boundary Precipitation Induced by Grain Crystallographic Misorientations in an Extruded Al-Mg-Si-Cu Alloy. *Journal of Alloys Compounds*, **624**, 27-30.  
<https://doi.org/10.1016/j.jallcom.2014.10.206>
- [13] Kliauga, A.M., Bolmaro, R.E. and Ferrante, M.J. (2015) The Evolution of Texture in an Equal Channel Pressed Aluminum AA 1050. *Materials Science and Engineering A*, **623**, 22-31. <https://doi.org/10.1016/j.msea.2014.10.073>
- [14] Ghosh, M., Miroux, A. and Kestens, L.A.I. (2015) Correlating R-Value and through Thickness Texture in Al-Mg-Si Alloy Sheets. *Journal of Alloys and Compounds*, **619**, 585-591. <https://doi.org/10.1016/j.jallcom.2014.09.038>
- [15] Shabadi, R., Suwas, S., Kumar, S., Roven, H.J. and Dwarkadasa, E.S. (2012) Texture and Formability Studies on AA 7020 Al Alloy Sheets. *Materials Science and Engineering A*, **558**, 439-445. <https://doi.org/10.1016/j.msea.2012.08.024>
- [16] Engler, O. and Hirsch, J. (2002) Texture Control by Thermomechanical Processing of AA 6xxx Al-Mg-Si Sheet Alloys for Automotive Applications—A Review. *Materials Science and Engineering A*, **336**, 249-262.  
[https://doi.org/10.1016/S0921-5093\(01\)01968-2](https://doi.org/10.1016/S0921-5093(01)01968-2)
- [17] Liu, W.C., Li, Z. and Man, C.S. (2008) Effect of Heating Rate on the Microstructure and Texture of Continuous Cast AA 3105 Aluminum Alloy. *Materials Science and Engineering A*, **478**, 173-180. <https://doi.org/10.1016/j.msea.2007.05.107>
- [18] Beese, A.M., Luo, M., Li, Y.N., Bai, Y. and Wierzbicki, T. (2010) Partially Coupled Anisotropic Fracture Model for Aluminum Sheets. *Engineering Fracture Mechanics*, **77**, 1128-1152. <https://doi.org/10.1016/j.engfracmech.2010.02.024>
- [19] Wang, X.F., Guo, M.X., Cao, L.Y., Luo, J.R., Zhang, J.S. and Zhuang, L.Z. (2015) Effect of Heating Rate on Mechanical Property, Microstructure and Texture Evolution of Al-Mg-Si-Cu Alloy during Solution Treatment. *Materials Science and Engineering A*, **621**, 8-17. <https://doi.org/10.1016/j.msea.2014.10.045>
- [20] Yang, X.H., Wang, D.G., Wu, Z.G., Yi, J.H., Ni, S., Du, Y. and Song, M. (2016) A Coupled EBSD/TEM Study of the Microstructural Evolution of Multi-Axial Compressed Pure Al and Al-Mg Alloy. *Materials Science and Engineering A*, **658**, 16-27.  
<https://doi.org/10.1016/j.msea.2016.01.080>
- [21] Huang, Y.C., Liu, Y., Li, Q., Liu, X. and Yang, C.G. (2016) Relevance between Microstructure and Texture during Cold Rolling of AA 3104 Aluminum Alloy. *Journal of Alloys and Compounds*, **673**, 383-389.  
<https://doi.org/10.1016/j.jallcom.2016.02.226>
- [22] Zhen, L., Chen, J.Z., Yang, S.J., Shao, W.Z. and Dai, S.L. (2009) Development of Microstructures and Texture during Cold Rolling in AA 7055 Aluminum Alloy. *Materials Science and Engineering A*, **504**, 55-63.  
<https://doi.org/10.1016/j.msea.2008.10.055>

- [23] Mishin, O.V., Bay, B., Winther, G. and Jensen, D.J. (2004) The Effect of Roll Gap Geometry on Microstructure in Cold-Rolled Aluminum. *Acta Materialia*, **52**, 5761-5770. <https://doi.org/10.1016/j.actamat.2004.08.028>
- [24] Lang, Y.J., Zhou, G.X., Hou, L.G., Zhang J.S. and Zhuang, L.Z. (2015) Significantly Enhanced the Ductility of the Fine-Grained Al-Zn-Mg-Cu Alloy by Strain-Induced Precipitation. *Materials and Design*, **88**, 625-631.  
<https://doi.org/10.1016/j.matdes.2015.09.023>
- [25] Gao, X. and Nie, J.F. (2007) Characterization of Strengthening Precipitate Phases in a Mg-Zn Alloy. *Scripta Materialia*, **56**, 645-648.  
<https://doi.org/10.1016/j.scriptamat.2007.01.006>



**Submit or recommend next manuscript to SCIRP and we will provide best service for you:**

Accepting pre-submission inquiries through Email, Facebook, LinkedIn, Twitter, etc.

A wide selection of journals (inclusive of 9 subjects, more than 200 journals)

Providing 24-hour high-quality service

User-friendly online submission system

Fair and swift peer-review system

Efficient typesetting and proofreading procedure

Display of the result of downloads and visits, as well as the number of cited articles

Maximum dissemination of your research work

Submit your manuscript at: <http://papersubmission.scirp.org/>

Or contact [jimmce@scirp.org](mailto:jimmce@scirp.org)